Kink instability and onset of critical regimes in a magneto-plasma-dynamic thruster

Gianluigi Serianni, Paolo Scarin, Matteo Zuin, Roberto Cavazzana, Emilio Martines, Matteo Agostini, Vanni Antoni, Mario Bagatin, Mariano Andrenucci, Fabrizio Paganucci, et al.

Kink instability and onset of critical regimes in a Magneto-Plasma-Dynamic Thruster

G Serianni†§, P Scarin† M Zuin† ‖, R Cavazzana† ,
E Martines† , M Agostini† , V Antoni† ‖, M Bagatin† ‖,
M Andrenucci‡¶, F Paganucci‡¶, P Rossetti‡ ¶ and M Signori‡

† Consorzio RFX, Associazione EURATOM-ENEA sulla Fusione, corso Stati Uniti 4, I-35127 Padova, Italy

‖ Istituto Nazionale di Fisica della Materia, Unità di Padova, Italy

‡ Department of Aerospace Engineering, University of Pisa, Via Caruso, I-56100 Pisa, Italy

¶ Centrospazio, Via A. Gherardesca 5, I-56014 Pisa, Italy

Abstract. Magneto-Plasma-Dynamic (MPD) thrusters are currently under investigation as they constitute a possible, high power electric propulsion option for primary space mission, ranging from orbit raising to interplanetary mission of large spacecraft. They are essentially electromagnetic plasma accelerators, in which a high current discharge ionises a gas, that is accelerated by the Lorentz force produced by the interaction between the current and a self induced (or applied) magnetic field.
Presently, the performance of this class of thrusters is limited by the onset of critical regimes observed when the current rises beyond a threshold value. In this regime, large fluctuations in the arc voltage signals and damages to the anode are observed along with thruster performance degradation. The present experimental investigation, carried out by several arrays of magnetic and electric probes and by two photomultiplier arrays of 16 channels each, has shown that the onset of these critical regimes is accompanied by the growth of large-scale MHD instabilities. These instabilities have m/n = 1/1 azimuthal and axial periodicity and have features of a helical kink mode. It has been found for the first time [1] that the threshold value for the current is well described by the Kruskal-Shafranov criterion currently applied in Thermonuclear Fusion research to interpret MHD stability of a screw pinch. The spatial structure of the kink has been reconstructed by the magnetic and electrostatic probes and preliminary results of the photomultiplier arrays for total radiation in the range 350-850nm confirms the helical structure of the kink.

1. Introduction

Magneto-Plasma-Dynamic thrusters are electromagnetic space propulsion devices, where the Lorentz force between a current and a magnetic field accelerates a plasma to high exhaust velocities (> 10 km/s) [2]. Due to the high thrust densities attainable with such devices, they constitute an attractive high power electric option for primary

§ To whom correspondence should be addressed (gianluigi.serianni@igi.cnr.it)

space missions, ranging from orbit raising to interplanetary transfers of large spacecrafts (Earth-to-Mars cargo and piloted missions) [3, 4]. The increasing trend in the available power onboard seems to make possible, on a shorter term, less ambitious missions concerning the transfer of heavier satellites of next generation from low earth orbit to geostationary earth orbit. For this class of missions, applied field magneto-plasma-dynamic (MPD) thrusters are more promising than self-induced devices, since they exhibit better performance at low power levels (some 10 kW). Currently the major limit on the use of MPD thrusters is their low efficiency, which has a maximum in the 20–40% range, while thrust efficiencies at least higher than 50% are required to make them preferable to chemical or other electric options.

However, the achievement of acceptable performance for space applications is hampered by the occurrence of detrimental phenomena, taking place when a critical current is exceeded [5]. This efficiency deterioration, which limits the MPD thruster performance, has been suggested to be due to the onset of critical regimes characterised by large fluctuations in the applied voltage signals and by damages to the anode [6]. These fluctuations have been interpreted in self-field MPDs in terms of plasma microinstabilities such as lower hybrid drift instability modified by finite-beta effects [7, 8] or space charge instabilities [6] and in applied field devices as shear Alfvén or compressional Alfvén waves [9, 10], resulting from the conversion of $m = 0$ and $m = 1$ magnetohydrodynamics (MHD) modes.

To the investigation of the role of plasma instabilities on the onset of critical regimes a great effort of theoretical and experimental studies is at present devoted, but the origin of the plasma phenomena regulating the thruster performance is still a matter of debate. Recently, in Ref. [11] the efficiency limits of self-field and applied-field MPD thrusters due to a non optimised use of the electromagnetic energy converted into thermic energy have been theoretically investigated.

The objective of this study is to investigate plasma instabilities growing in current regimes both below and above the critical value, to get insight on the nature of the plasma phenomena, and their relationship with the thruster performance degradation. In particular, plasma instability properties have been investigated both with and without the application of the external magnetic field, whose role, to our knowledge, has never been previously discussed.

The paper is organised as follows: in section II the experimental equipment is described, in section III the properties of plasma fluctuations are analysed. Section IV is devoted to the discussion of the experimental results and to the comparison with theoretical predictions for the MHD instabilities in a plasma column.

2. The Experimental Equipment

2.1. The Magneto-plasma-dynamic Thruster

A schematic of the MPD thruster object of the present investigation is shown in Fig. 1. This device is named Hybrid Plasma Thruster (HPT). A cylindrical system of coordinates is introduced, where $z = 0$ is located at the thruster outlet.

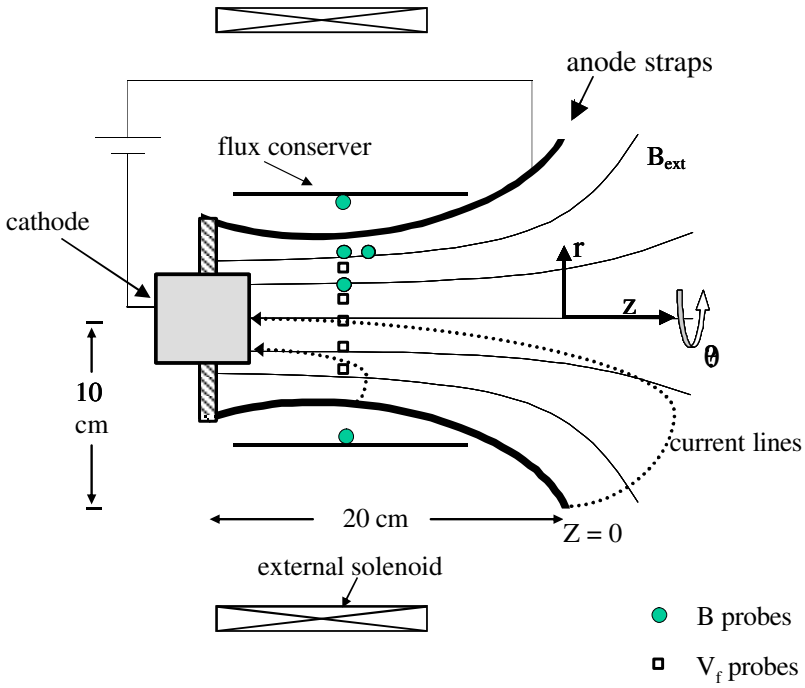

Figure 1. Schema of the HPT, showing shape of the anode straps, external magnetic field lines, external solenoid, magnetic and electric probes position and two examples of current lines.

The HPT is an axisymmetric MPD thruster with a central hollow multichannel cathode. The multichannel cathode consists of 19 copper tubes with external diameter of 8.5 mm and thickness of 0.5 mm; they are housed inside a holder tube whose external diameter and thickness are respectively 44 mm and 1.3 mm. The total cross section area useful for the gas passage is about 1100 mm^2. The choice of a multichannel cathode is justified in that, with respect to more conventional configurations like rod or single-channel cathode, this type of cathode exhibits a lower erosion rate, which is an important aspect for steady MPD thruster application, and a larger operating range in terms of mass flow rate and current values.

The anode consists of eight copper straps which collect most of the current, each 20 mm wide, equally spaced in the azimuthal direction, shaped as shown in Fig. 1. An

aluminium cylinder (150 mm diameter, 100 mm length, 5 mm thickness), electrically insulated from all the electrodes and mounted coaxially to the thruster, surrounds the anode straps acting as a flux conserver for the plasma column. The system is bounded by a copper cylinder (200 mm diameter, not shown in the scheme of Fig. 1) electrically connected to the anode straps. (More details on the experimental equipment can be found in Ref. [5]).

The electric power is supplied by a Pulse Forming Network (PFN), which allows quasi-steady current pulses (I_{tot}) lasting 2.5 ms. By means of an external solenoid, powered by a dc generator, an axial magnetic field (B_{ext}) up to 100 mT can be applied on the thruster axis. The dc generator is switched on few seconds before the discharge, so that B_{ext} can be considered stationary during the discharge. It is important to note that magnetic field lines do not link the cathode and the anode, as indicated in Fig. 1.

The propellant is injected by two gas feeding systems, one for the central cathode and the other for eight peripheral injectors equally spaced in the azimuthal direction, located between the anode straps and the external cylinder. The feeding system is based on fast acting solenoid valves, which provide gas pulses with a long plateau after few milliseconds from valve activation. When a steady state mass flow is reached, the discharge takes place by switching on an ignitron, which closes the electric circuit at $t = 0$. Unless otherwise stated, for the experiments described in this paper Argon is used as main propellant at a mass flow rate of 660 mg/s, distributed in the ratio of 10:1 between the central and peripheral valves respectively.

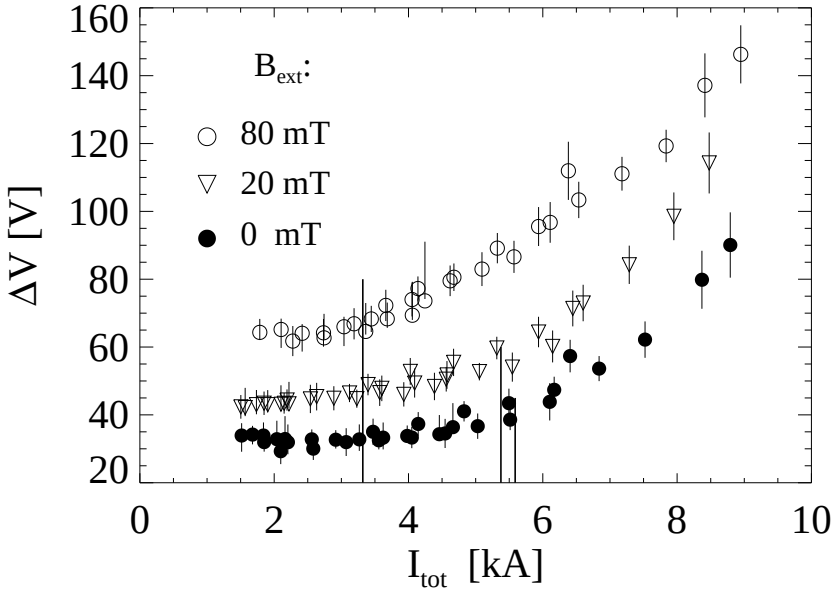

Figure 2. Electrical characteristic (ΔV vs I_{tot}) of the discharge for different B_{ext} values. Error bars are obtained by averaging over different shots. The dashed vertical lines mark the critical current values predicted by eq. 1 for each experimental condition.

In Fig. 2 the electrical characteristic of the thruster operation is shown, for different values of the externally applied field. Current and voltage measurements show a good reproducibility (the small error bars being due to the average of different shots). In Fig. 2 a change in slope of the I-V curve can be seen, at a current level which decreases by increasing the applied B_{ext}. Such a change is usually identified as the onset condition for the critical regimes, above which the efficiency of the thruster is degraded due to the rapidly increasing power required to sustain the discharge. By varying the discharge current I_{tot} in the range $1.5 - 9$ kA, and applying a B_{ext} in the range from 0 to 100 mT, a wide range of critical and non-critical regimes has been explored in the experiments described in this paper. The thruster has been operated in power regimes spanning from 45 kW to 1.6 MW. The PFN has been charged in a range from about 400 to 1350 V, while the voltage difference between the anode and the cathode spans from 30 to 180 V after breakdown.

The vertical lines overplotted in Fig. 2 refer to the threshold current I_{cr} for critical regimes predicted by a semi-empirical model [12]. This model, for the case of the applied field MPD, expresses I_{cr} as a function of the geometrical properties of the thruster and of the plasma parameters:

$$I_{cr} = \frac{\mu_0 C_s \dot{m} A_{0cr}}{B(R_a - R_c) \times 10^{-7}} \tag{1}$$

where C_s is the ion-sound velocity, $\dot{m}$ the mass flow rate, B the total magnetic field at the cathode tip, R_a and R_c are the anode and cathode radii respectively, and A_{0cr} an empirical parameter ($A_{0cr} = 3.6/[(R_a/R_c) - 0.5]$). All quantities are expressed in SI units. For the case of the self-field MPD ($B_{ext} = 0$), the functional form for the I_{cr} is only slightly different [12]. With the typical plasma parameters measured in the thruster, $n_e \approx 10^{20}$ m^{-3} and $T_e \approx 5 - 10$ eV [13], the above expression leads to a threshold in current for critical regimes ranging from 4 kA to 6 kA with $B_{ext} = 40$ mT, whereas I_{cr} is around 5.5 kA for the self-field case. These values are in rather good agreement with the experimental results (see Fig. 2).

All experimental conditions were replicated with a reversed external field. Few experimental conditions were also explored using Helium instead of Argon as propellant gas in order to investigate the dependence of the fluctuations properties on the ion mass. Because of the limitation due to the Paschen ionisation curve [14], it has been possible to explore only current regimes above the critical value, which for Helium is less than 1.4 kA, according to eq. 1. Whenever not explicitly declared we will hereafter refer to discharges in Argon gas.

The device is mounted on a thrust stand inside a vacuum chamber ($length = 3.5$ m, $radius = 0.6$ m), electrically insulated from both electrodes, which maintains a back pressure of the order of 10^{-2} Pa during the pulse. The chamber is large compared to the plasma dimensions, which leads to the hypothesis that boundary effects are not crucial in determining the discharge behaviour.

2.2. Set-up of diagnostic systems

Different arrays of magnetic, electric and optical probes have been used in order to investigate the space-time properties of the plasma fluctuations. The estimated bandwidth for electrostatic and optical measurements is limited to about 500 kHz, whereas for magnetic signals it extends up to ∼6 MHz. For electrostatic and magnetic sensors, the acquisition sampling frequency was 20 MHz; for optical signals, 10 MHz was adopted. A schematic of the two insertable systems can be found in Fig. 3, together with a picture of one of the small three-axial magnetic coils.

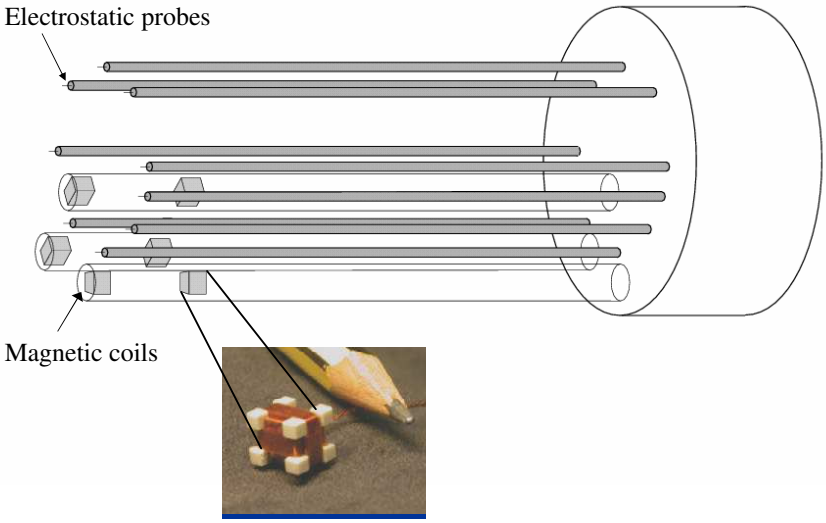

Figure 3. Schema of the insertable diagnostic system. In the small picture the particular of a three axial magnetic coil is shown.

2.2.1. Magnetic Sensors The first system consists of six three-axial magnetic coils housed in quartz tubes, each tube containing two probes spaced by 15 mm. All quartz tubes have been inserted parallel to the main axis, two of them located at $r = 41$ mm, azimuthally spaced by $\pi/4$, the third at $r = 18$ mm. The most inserted sensors have been located in two different axial positions: at $z = -109$ mm, i.e. in the point where the vacuum magnetic flux tubes have the minimum diameter, and at $z = 0$ mm (see Fig. 1). Each probe consists of three coils wound with 0.2 mm diameter wire on a small parallelepiped-shaped support (7 by 7 by 8 mm).

The second diagnostic system consists of four external two-axial magnetic coils, mounted on the inner surface of the flux conserver at $z = -109$ mm, measuring axial and azimuthal magnetic fluctuations in four equally spaced azimuthal positions (see Fig. 1). Where not explicitly specified the internal measurements obtained at $z = -109$ mm will be presented.

2.2.2. Electrostatic Sensors A circular array of eight equally spaced electrostatic sensors has been used, with 31 mm radius, which has been placed in the same axial positions as the most inserted magnetic probes, i.e. at $z = -109$ mm and $z = 0$ mm. Each probe is a tungsten wire, 1 mm radius, 2 mm long, housed in a quartz tube and has been used for floating potential measurements. The floating potential V_f is related to the plasma potential V_p and to the electron temperature T_e by

$$V_f = V_p - \alpha T_e \tag{2}$$

where α is a positive constant [15]. Previous experiments performed in this kind of thruster by means of triple Langmuir probes have shown that electron temperature fluctuations exhibit the same spectral properties as floating potential (and density) fluctuations [16]. As commonly done in other systems [17], temperature fluctuations have been thus neglected in this context, so that floating potential fluctuations are considered as representative of plasma potential fluctuations.

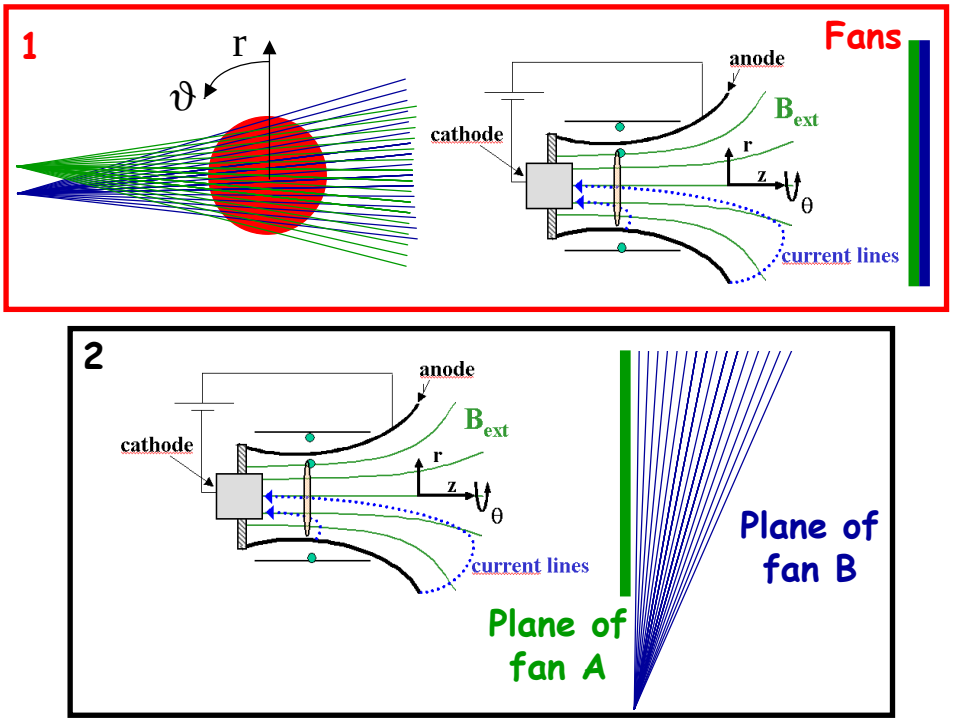

Figure 4. Schema of optical diagnostic and experimental set-up.

2.2.3. Optical Diagnostic An optical diagnostic system has been used to view the thruster plume. The optical system comprises two fans which have been arranged in two different configurations, as shown in Fig. 4. In the diagnostic arrangement no. 1, the fans intersect each other at an angle of 7 deg in a plane perpendicular to the thruster plume; this arrangement will make it possible to evaluate the two-dimensional pattern of emitted radiation. Such a work is in progress. With the second arrangement, the simultaneous investigation of emitted radiation can be carried out both on the plane

perpendicular to the thruster plume and along the axial direction, though it must be always born in mind that the optical signals are line-integrated. Only results from the second arrangement will be presented in the present paper.

Each fan spans 10 deg and comprises sixteen lines of sight. In the focal region the spacing between adjacent lines of sight is 9 mm and the beams have a diameter of 7 mm. The light is collected by the optics (focal length 85 mm, f-number 11 for fan A and f-number 16 for fan B), located outside the vacuum chamber, after passing through the vacuum window and an attenuating neutral filter (attenuation factor equals to 1000 and 4000 for fan A and B respectively), and reaches two detectors equipped with a 16 channel photomultiplier array Hamamatsu 5900U-20-L16 each. The current-to-voltage converters developed for this application are based on OP-37 operational amplifiers, configured as transimpedance converters with a gain of 20 mV/μA. At this gain the equivalent noise input level generated by the converter is of the order of the dark current of the PMT sensor and the analog bandwidth is 1.8 MHz. A further gain/buffer stage amplifies the signal by a factor between 2 and 5 [18].

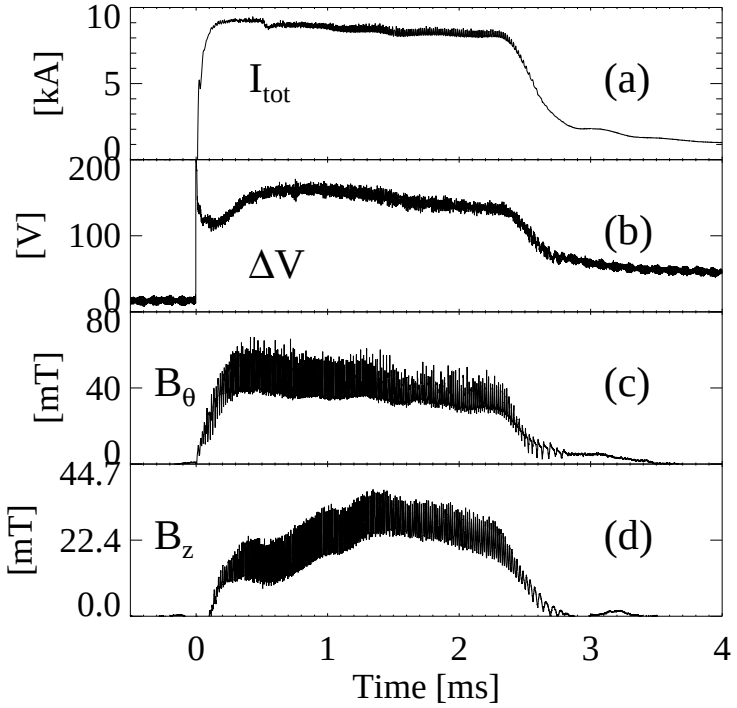

Figure 5. Time history of a typical discharge: (a) total current I_{tot}, (b) potential difference between anode and cathode ΔV, (c) azimuthal magnetic field B_ϑ measured at $r = 41$ mm, (d) axial magnetic field B_z measured at $r = 18$ mm. $B_{ext} = 100$ mT and $I_{tot} = 9$ kA.

3. Plasma fluctuation properties

Typical waveforms of the discharge current I_{tot}, the voltage difference between anode and cathode ΔV, the azimuthal magnetic field B_ϑ measured by the insertable probe at $r = 41$ mm and the axial magnetic field B_z at $r = 18$ mm are shown in Fig. 5. All the magnetic quantities have been obtained through a numerical integration of the probe signals. Since sampling starts after the externally applied axial field is switched on, the B_z signal does not include such field, which, as already mentioned, is constant throughout the discharge.

Two important features can be observed in Fig. 5. The first is that a large positive B_z of about 25 mT is induced by the plasma close to the thruster axis after the start of the plasma current ($t > 0$). Thus, the externally applied field ($B_{ext} = 100$ mT in this case) is significantly increased, which means that the discharge has a paramagnetic behaviour. The second important feature is the presence of strong fluctuations on all signals during the discharge. The latter feature is confirmed by the optical signals, an instance of which is presented in Fig. 6. Notice that the optical diagnostic was used in discharges with duration of 5 ms, unlike the other measurements.

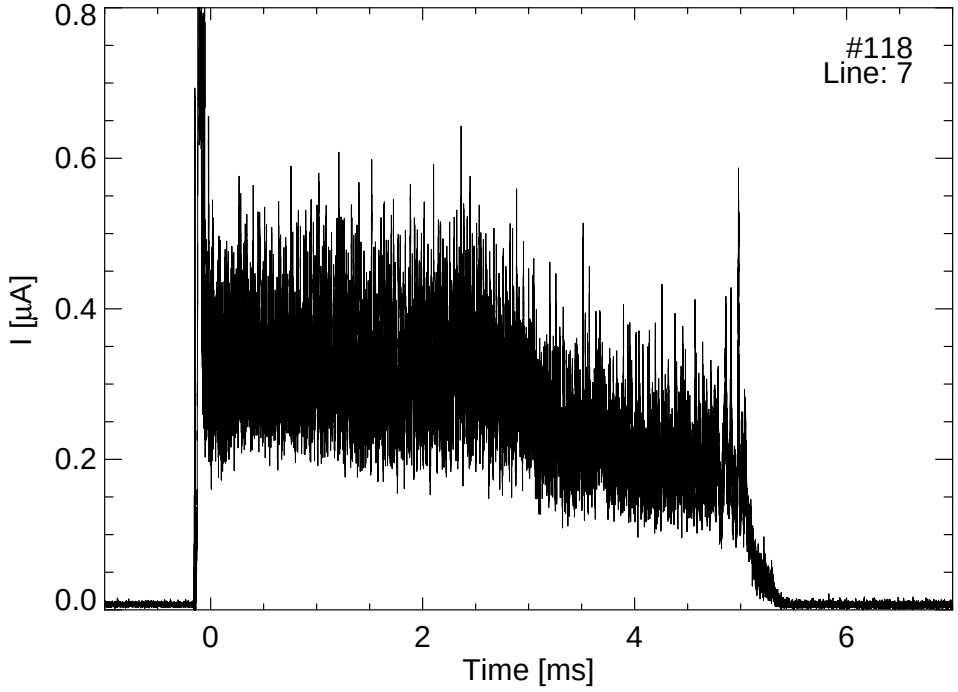

Figure 6. Time history of line of sight number 7, in the centre of the fan ($B_{ext} = 100$ mT, $I_{tot} = 9$ kA, mass flow rate 120 mg/s).

Figure 7 shows the temporal behaviour of the four external B_z measurements and of the inner measurements of B_r, B_ϑ and B_z, together with the eight floating potential signals. A regular oscillation at about 100 kHz can be seen in all signals, both for magnetic and electrostatic measurements. A well defined phase difference between the probes is observed, implying an azimuthal propagation (rotation) with the same angular

velocity for the inner electrostatic array of probes and the external magnetic array. These findings confirm the electromagnetic nature of the process under consideration.

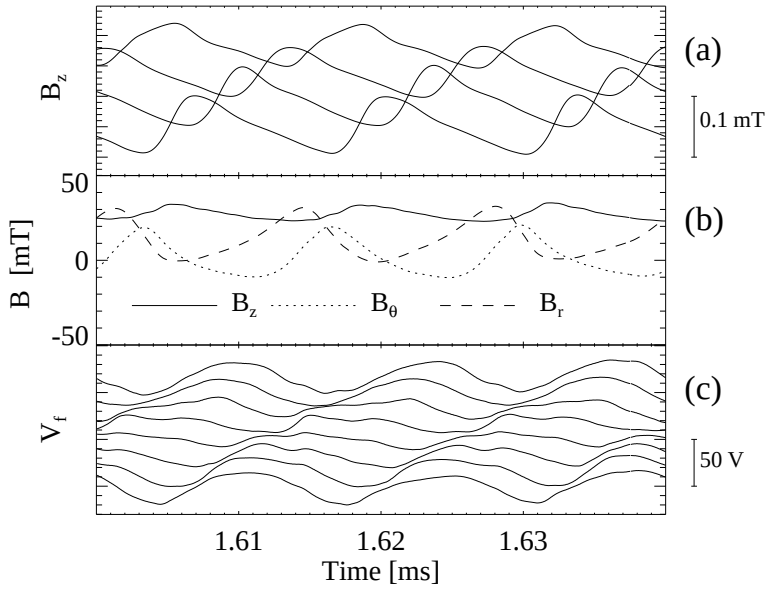

Figure 7. Temporal evolution of: (a) 4 B_z signals close to the flux conserver, (the scale refers to one signal, the others having been vertically shifted), (b) B_r, B_ϑ, B_z measured at $r = 18$ mm, (c) eight V_f signals (vertically shifted). $B_{ext} = 100$ mT and $I_{tot} = 8$ kA.

In Fig. 8 the power spectrum of a single floating potential signal measured at $r = 41$ mm in three different experimental conditions (with Argon at $z = 0$ and $z = -109$ mm, and with Helium at $z = -109$ mm) is plotted. Figure 9 displays the power spectrum of the optical signal corresponding to line of sight 12, lying on the external side of the fan. The power spectrum of a generic signal, $x(t)$, has been computed by dividing the x(t) signal into N slices of equal length, and using each of them as an independent realisation of the process under study, as required for a statistically meaningful result [19]. Each slice has been multiplied by the Hanning window so as to reduce leakage. Fig. 8 confirms, in the frequency range explored, the presence of a dominant oscillation for the inner ($z = -109$ mm) measurements at about 100 kHz.

Such a result cannot be explained by the LHCDI theory [7]. Lower hybrid instability should operate near the lower hybrid frequency f_{LH}, which falls between the electron cyclotron f_{ce} and the ion cyclotron f_{ci} frequencies ($f_{LH} \cong (f_{ce} f_{ci})^{1/2}$, where $f_{ci,e} = \frac{eB}{2\pi m_{i,e}}$). For the case under study ($B_{ext} = 100$ mT), upon considering a total magnetic field $B > 100$ mT, f_{LH} results higher than 10 MHz, at least two orders of magnitude larger than the frequency of the oscillation observed on all signals. It must be said that the expected f_{LH} would be very close, or even above, the Nyquist's frequency and surely higher than the upper estimated bandwidth limit ($\sim$ 6 MHz as already

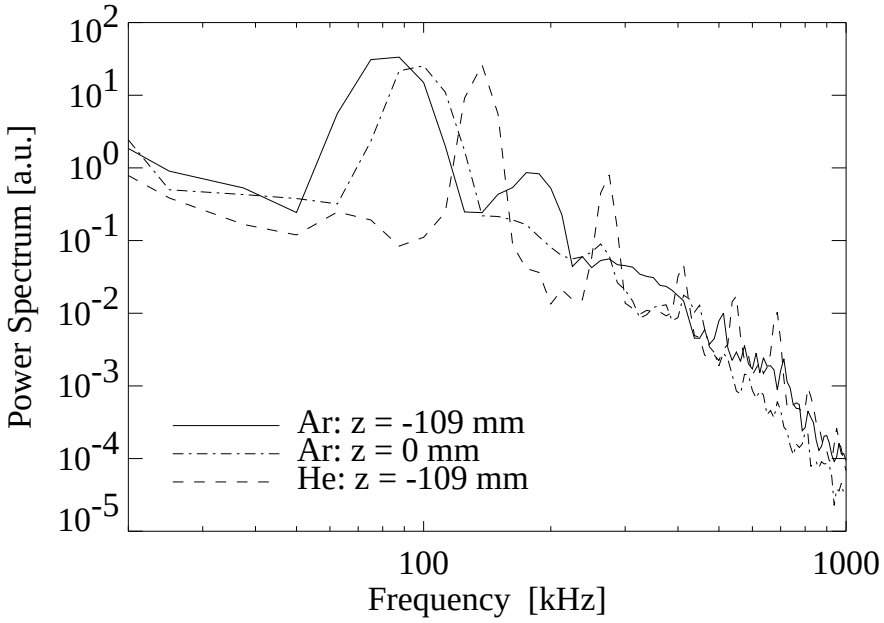

Figure 8. Power spectra of a floating potential signal for three different experimental conditions ($B_{ext} = 100$ mT and $I_{tot} = 8$ kA).

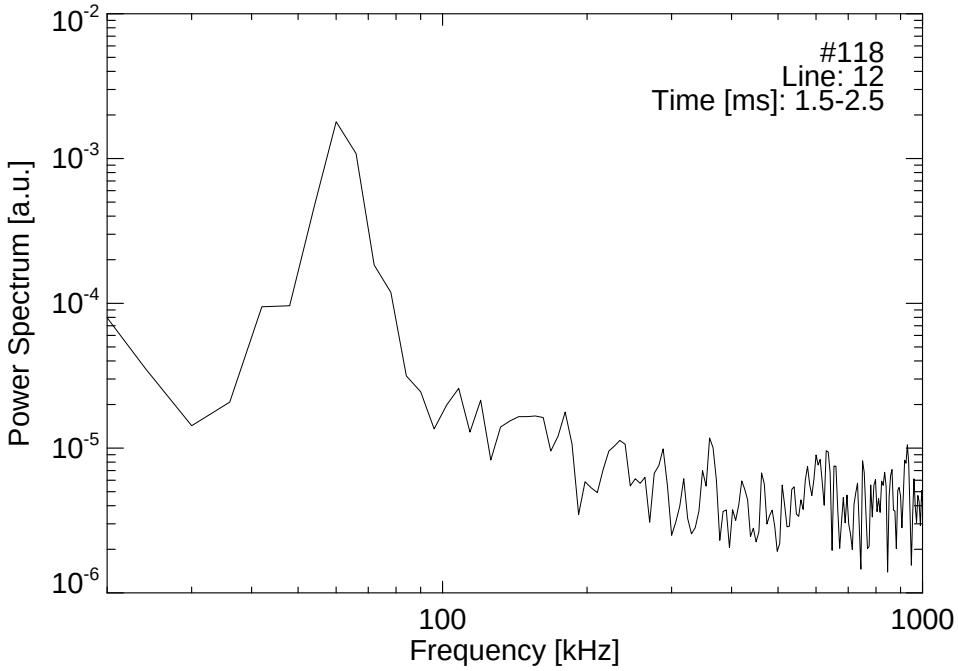

Figure 9. Power spectra of optical signal corresponding to line of sight 12 ($B_{ext} = 100$ mT, $I_{tot} = 9$ kA, mass flow rate 120 mg/s).

mentioned) for the probes. Though the development of LHCDI cannot be excluded, for the limited frequency bandwidth of the measurements, we can however conclude that the dominant oscillation, in the frequency range explored, is not a signature of LH

instability. In particular the use of the much lighter Helium gas ($\frac{m_{Ar}}{m_{He}} \simeq 10$), for similar values of the local magnetic field, has shown an increase of the dominant frequency (see Fig. 8), but not a scaling with $m_i^{-1/2}$, as would be expected by the LHCDI theory. Moreover it is important to note that almost the same frequency is observed on the signals from measurements at $z = 0$ mm (Fig. 8) and even in the thruster plume (Fig. 9), where, because of the decreasing of both B_ϑ and B_z components [5], the total magnetic field is at least one order of magnitude lower.

A spatial Fourier decomposition technique has been applied to the eight electrostatic signals, belonging to the circular array, to investigate the spatio-temporal pattern of fluctuations, obtaining the time behavior of mode amplitudes and phases. The amplitudes $a_m(t)$ and the phases $\alpha_m(t)$ are related to the measured field x(t) (in this case the floating potential) by

$$x(\vartheta, t) = \sum_{m=0,1...} a_m(t) cos[m\vartheta + \alpha_m(t)] \tag{3}$$

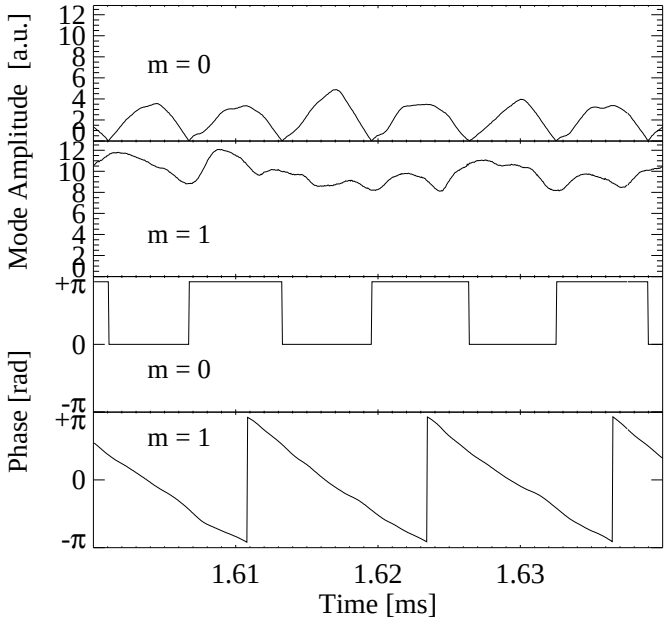

Figure 10. Temporal evolution of the amplitude of the $m = 0$ and $m = 1$ azimuthal modes and their phases, as obtained from the floating potential measurements ($B_{ext} =$ 100 mT and $I_{tot} = 8$ kA.

In practice, amplitudes and phases are computed by applying the Fast Fourier Transform (FFT) algorithm to the 8 electrostatic measurements at each sampling time. Nyquist's sampling theorem restricts the mode number range to $m = 0 \div 3$, while for $m = 4$ only part of the total mode amplitude can be recovered. The typical time evolution for $m = 1$ and $m = 0$ modes amplitude, during the stationary part of the discharge is shown in Fig. 10 together with their phases. The largest amplitudes are

obtained for the lowest order modes ($m = 1$ and $m = 0$), which grow few microseconds after $t = 0$ and then oscillate during the plateau phase. Higher order modes ($m > 1$) normally exhibit almost negligible amplitude. It is found that $m = 1$ is the dominant azimuthal periodicity and the linear dependence of the phase on time confirms the rotation at a frequency of about 100 kHz. The $m = 0$ pulsates almost sinusoidally with the same frequency of the $m = 1$.

Similar results are obtained from the line-of-sight–integrated optical measurements in Fig. 11, by computing half the sum and half the difference between lines of sight 5 and 14. The specific lines have been chosen as the ones which look symmetrical with respect to the thruster plume, probably due to some equipment misalignment.

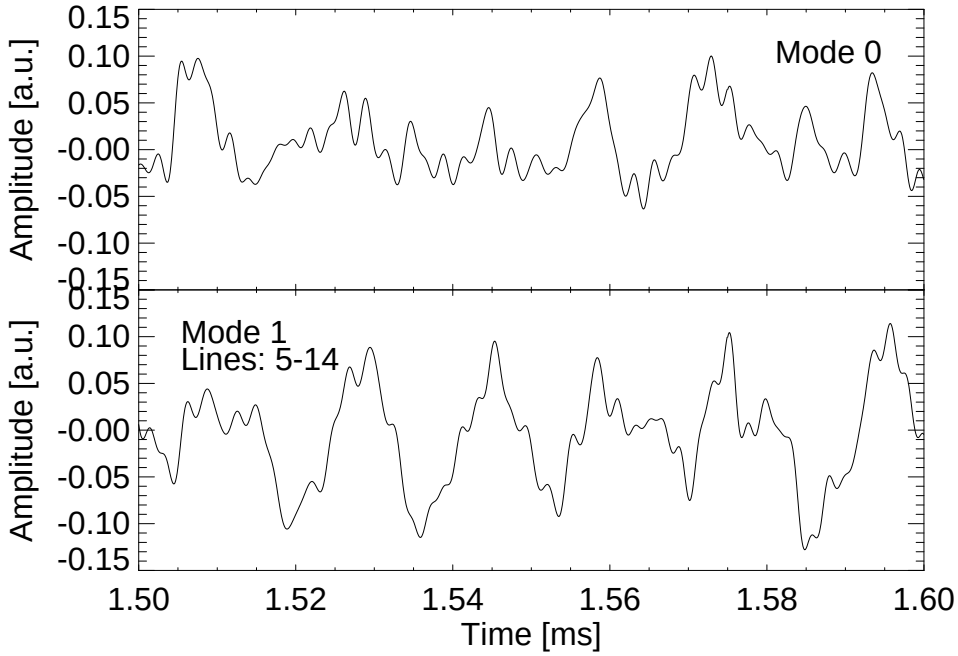

Figure 11. Temporal evolution of the amplitudes of the $m = 0$ and $m = 1$ azimuthal modes, as obtained from the optical measurements ($B_{ext} = 100$ mT, $I_{tot} = 9$ kA, mass flow rate 120 mg/s).

The $m = 1$ mode frequency shows a linear dependence on I_{tot} (ranging from 30 to 100 kHz for $1.5 < I_{tot} < 9$ kA, corresponding to a rotation velocity of about 20 km/s measured at $r = 41$ mm), whereas it has only a weak dependence on B_{ext}. The propagation direction changes sign when the external field is reversed and is consistent with that of the $\mathbf{E} \times \mathbf{B}$ drift of the particles.

A comparison of frequency and amplitude measurements performed by means of the external probes with and without the insertion of the internal diagnostic system have shown that its presence does not significantly modify the plasma dynamics.

Figure 12 shows the total energy of the $m = 0, 1$ modes as a function of I_{tot} for the cases with $B_{ext} = 0, 10, 100$ mT. The mode energy is time averaged over 1 ms during the plateau phase. It can be noticed that the time-averaged amplitude of the dominant $m = 1$ mode depends on I_{tot} and B_{ext} values. At the highest current the averaged

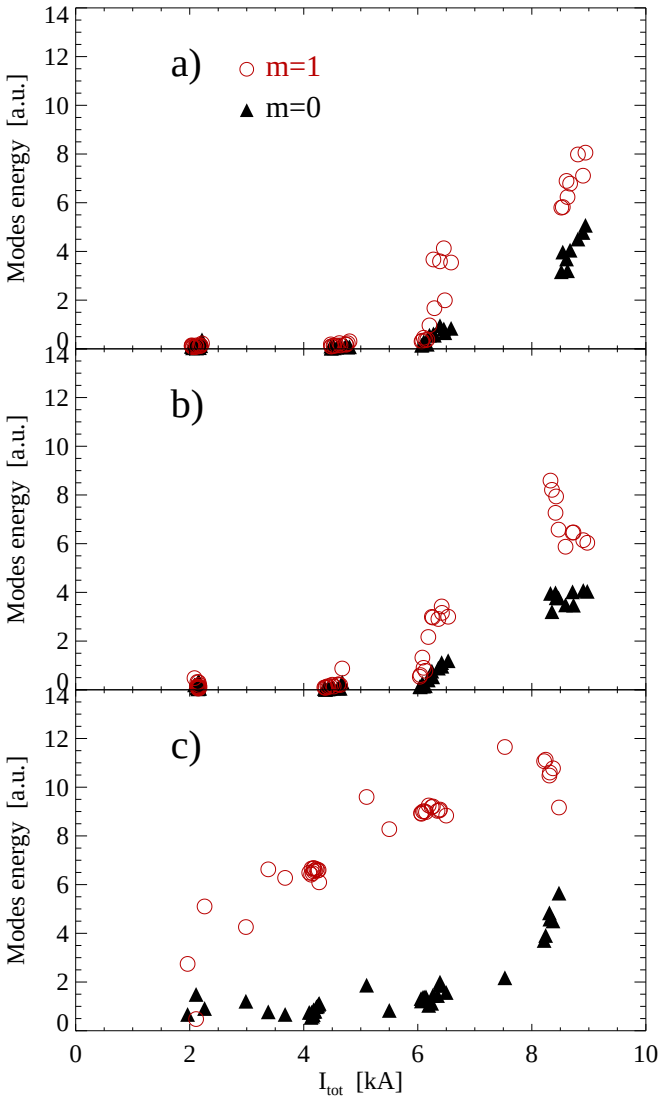

Figure 12. Energy of $m = 0$ and $m = 1$ modes, as a function of the I_{tot}, averaged over time during the plateau phase (∘) for: a) $B_{ext} = 0$, b) $B_{ext} = 10$ mT, c) $B_{ext} = 100$ mT.

amplitude of the $m = 0$ mode increases, being comparable to the amplitude of the $m = 1$ mode at low B_{ext} values. As an example, for low B_{ext} values the mode energy is almost zero for $I_{tot} < I_{cr} \simeq 5.5$ kA and the $m = 1$ amplitude jumps to high positive values when the current rises beyond the critical value. At high applied field, $B_{ext} = 100$ mT for the case in Fig. 12c, the critical condition appears at lower current, so that the mode amplitude is low only for $I_{tot} \leq 2$ kA, and increases with increasing power.

In order to get more insight into the nature of this instability, the axial structure of the mode has been analysed by means of two axially spaced magnetic probes, located at $r = 41$ mm. The spectral density S(k_z,f), where k_z is the wavevector in the axial direction and f is the frequency, has been deduced by means of a two-point statistical technique [20, 21]: the signals y_1 and y_2 of the two probes are divided into N slices of equal length, $y_1^{(i)}$ and $y_2^{(i)}$ ($i = 1...N$). The slices are considered as independent realisations of the stochastic process under study. For each slice, the discrete Fourier transforms $\Psi_1^{(i)}(f)$ and $\Psi_2^{(i)}(f)$ are computed. From these, the power $S^{(i)}(f) = (\mid \Psi_1^{(i)}(f) \mid^2 + \mid \Psi_2^{(i)}(f) \mid^2)/2$ and the cross-phase $\alpha^{(i)}(f) = arg([\Psi_1^{(i)}(f)]^* \Psi_2^{(i)}(f))$ are computed. The cross-phase is used to obtain an estimate of the wavenumber in the direction connecting the two probes, $k_z^{(i)}(f) = \frac{\alpha^{(i)}(f)}{\Delta z}$, where Δz is the distance between the probes. These results are used to progressively fill a histogram of the spectral density, i.e., for each frequency f, the bin corresponding to the wavenumber $k_z^{(i)}(f)$ is increased by the amount $S^{(i)}$(f). The spectral density function S(k_z,f) is obtained by repeating this procedure for all slices. In this analysis, stationarity of the process and Δz much smaller than the fluctuation axial wavelength are assumed. The S(k_z,f) for the probes measuring the radial component of the fluctuating magnetic field is shown in Fig. 13, for $B_{ext} = 100$ mT.

The most prominent feature of the plot is the presence of a relatively sharp peak appearing at the main oscillation frequency of the signals (also higher harmonics can be observed), corresponding to a single discrete wavevector. Values of k_z ranging from 10 to 60 m^{-1} have been obtained, which imply wavelengths from about 0.1 to 0.6 m. Measurements in different experimental conditions (I_{tot} and B_{ext}) have confirmed the almost linear increase of the frequency with the current (as already mentioned) and have shown that the axial wavelength λ_z increases with B_{ext}. In particular, as shown in Fig. 14, the longest wavelengths have been estimated for the largest B_{ext}. It is important to note that only discrete wavevectors have been detected, while a continuum of wavelengths would be expected in an open system. The configuration 2 of the optical measurements provided a confirmation of the values of the measured λ_z.

Similar results have been found in other open devices [22] and a possible explanation for this is proposed, for example, in Ref. [23], which suggests that a local discontinuity on the Alfvén velocity ($v_A = \frac{B}{(\mu_0 \rho)^{1/2}}$, where ρ is the mass density of the used gas) can act as a virtual axial boundary for the system.

Optical measurements in high B_{ext} regimes [13] show that the plasma plume extends up to 0.4 m outside from the thruster outlet. Therefore the result of the total axial length of the plasma column L is about 0.6 m, comparable to the axial wavelength measured

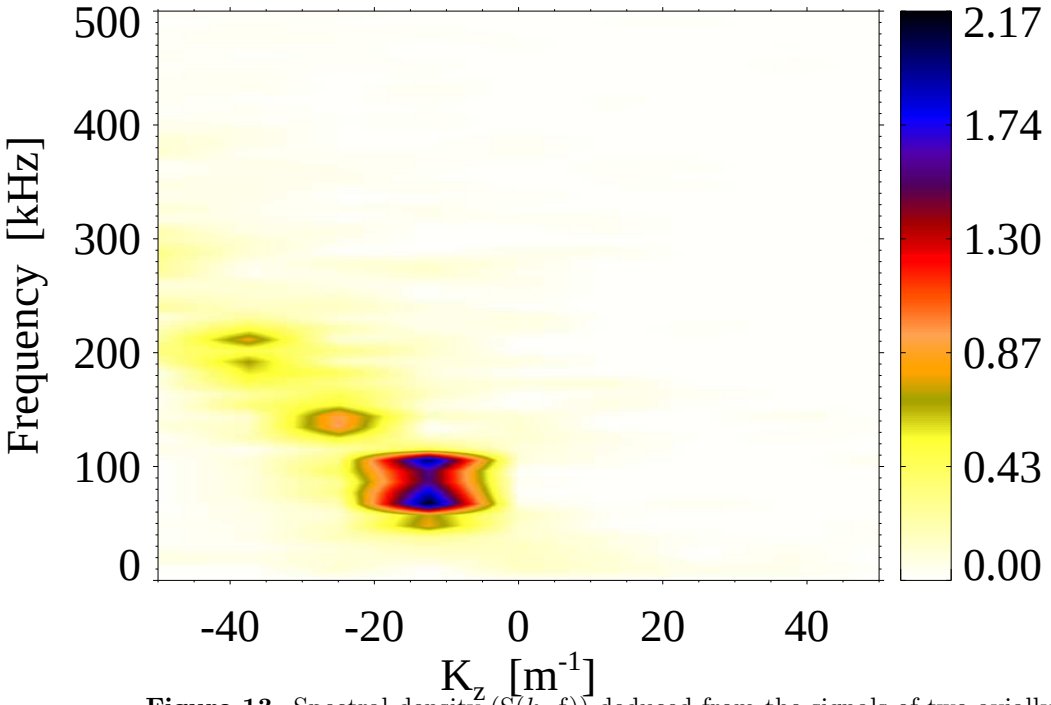

Figure 13. Spectral density (S(k_z,f)) deduced from the signals of two axially spaced magnetic probes, measuring the radial component of the fluctuating magnetic field B_r ($B_{ext} = 100$ mT and $I_{tot} = 8$ kA).

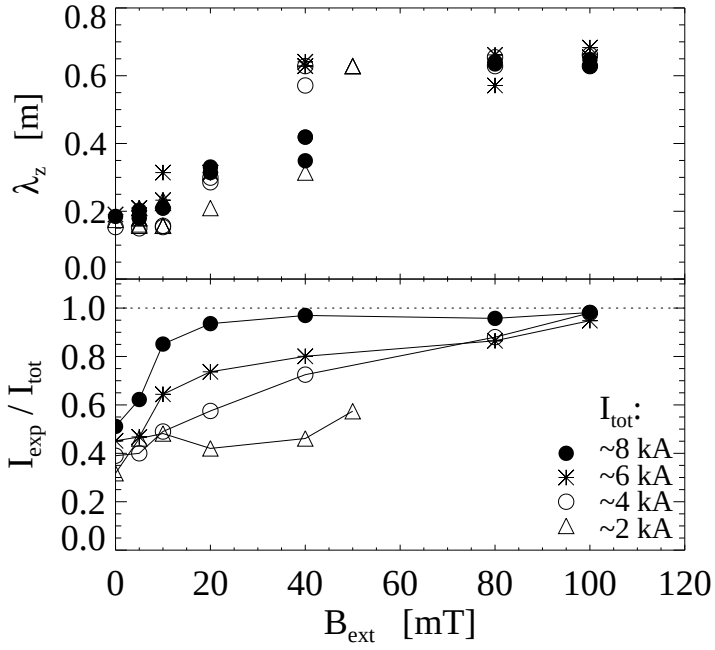

Figure 14. Axial wavelength (top) and ratio between the measured I_{exp} and I_{tot} (bottom) plotted as a function of B_{ext}, for four different total current regimes.

in the same experimental conditions. As a consequence the mode results in winding once azimuthally for an equivalent $n = 1$ axial periodicity. This leads to the conclusion

that the mode is a $m/n = 1/1$ helical kink mode [24]. Another analogy can be noticed between the HPT and the system of Ref. [22], in that the pitch of the kink is not constant: indeed, the optical measurements in the configuration depicted in Fig. 4 give a wavelength in the axial direction of about 1 m, by applying the same technique described earlier.

4. Discussion

4.1. The helical kink mode

By combining applied field and mostly parallel current, the applied-field MPD thruster can be placed within a wide category of devices, which could generally be labelled as screw pinches [25]. A general feature of screw pinches is that when some threshold of the ratio between current and applied magnetic field is exceeded, current driven large scale MHD instabilities are excited, with effects which range from distortion or changes in the topology of the discharge to its disruption [25]. A peculiar feature of many of such systems is that such MHD instabilities can lead to an amplification of the applied magnetic flux, linked to a spontaneous reorganisation of the current density pattern inside the device [26, 27]. This process is predicted by Taylor's theory [28] for systems relaxing to minimum energy state and constrained to a constant total magnetic helicity. This is usually labelled as dynamo effect.

It is worth emphasising that the present discussion focusses on the effects due to the current component parallel to the applied magnetic field, rather than on the purely cross field (radial) component, which is usually taken into account to explain the current driven micro instabilities, such as the LHCDI. It is however interesting to note that some studies [29], aimed at investigating the role of the generalised lower hybrid drift instability (GLHDI), of which LHCDI is a special case, in Harris current sheet equilibrium [30], have shown that long wavelength drift-kink current driven modes can grow after the excitation and saturation of the shorter wavelength and higher frequency LH mode. It must be said that Harris current sheet geometry is quite different from cylindrical plasma column, but the underlying physics is closely related.

The case of the self-field MPD thruster would be topologically different from the applied field version. It is however experimentally known that at high current the discharge usually presents a spontaneous breaking of the axial symmetry [31]. In these situations the generation of an axial magnetic field component, though small, is expected. Therefore the self-field operations, at least for high current conditions, can be compared to the low B_{ext} applied field operations. This approximation is further reinforced by the experimental observation that the fluctuation properties obtained for $B_{ext} = 0$ and $B_{ext} \leq 10$ mT are quite similar.

In the screw pinch topology, a perturbation for the system, which could be one of the several normal modes supported by MHD equations, may be characterised by a

two-dimensional wave (propagation) vector **k**, and can be written in the form

$$f(\mathbf{r}) = f_k(x)e^{i\phi(y,z)} \tag{4}$$

where **r** is the position vector, the planes $x = constant$ are those where the field lines lie and $\phi = \mathbf{k} \cdot \mathbf{r}$ is the phase of the perturbation. The wavefronts of this perturbation are defined by the condition $\phi = constant$ and can be thought of as surfaces of constant displacement. The effect of such a displacement is to cause a magnetic field bending, which results in a stabilising effect [25]. If the wavefronts of the perturbation and the unperturbed magnetic field lines have the same pitch, the resonance condition

$$\mathbf{k} \cdot \mathbf{B} = \mathbf{0} \tag{5}$$

is satisfied and the stabilising effect vanishes.

For a cylindrical plasma column of length L and radius r, where the coordinates become $x \rightarrow r$, $y \rightarrow \vartheta$, the **k** components are restricted to assuming discrete values $k_\vartheta = m/r$ and $k_z = n\frac{2\pi}{L}$, with m and n integers (m and n are the azimuthal and axial mode numbers, respectively). The unperturbed magnetic field lines lie on surfaces of constant radius, and flux surfaces appear as nested, concentric cylinders. On each surface magnetic field lines will be helices in space, whose pitch is determined by the ratio B_ϑ/B_z.

In cylindrical coordinates eq. 5 can be rewritten in terms of the safety factor q, which is a function of the radius, $q(r) = \frac{2\pi r B_z}{L B_\vartheta}$, as $q(r) = -m/n$. Magnetic surfaces where this condition is satisfied are dubbed resonant (or rational) surfaces. It is known from the studies on toroidal plasma confinement for thermonuclear fusion that one of the most dangerous instabilities for a plasma column is the $m/n = 1/1$ kink mode. For its stability the Kruskal-Shafranov condition requires $q > 1$ at each radius [27]. A class of thermonuclear toroidal devices that satisfy this criterion is the tokamak. Unlike tokamaks, in the reversed-field pinch (RFP) the value of q on axis is $q(0) < 1$ and decreases to a slight negative value at the edge. Therefore the presence of the m/n=1/1 kink mode is avoided altogether by a magnetic topology which implies $q(r) < 1$ everywhere.

As given in Ref. [26] an $m/n = 1/1$ kink instability, resonant on the $q = 1$ surface, has been demonstrated to be the mechanism of the toroidal flux amplification in a fast pinch experiment. The growth of a helical perturbation is shown to depend on the presence of a $q = 1$ resonant surface in the plasma column at some radius.

In the HPT the situation is more complex than in an ideal screw pinch, due to the presence of a radial current density, which allows the current to flow from the anode to the cathode. As a consequence, the axial current is not constant along the plasma column, but is a decreasing function of the axial position z. For the present analysis, the axial current I_{exp} at the probe axial position has been directly obtained by measuring B_ϑ close to the anode and applying Ampere's law, with the assumption of azimuthal symmetry.

In Fig. 14 the ratio of the measured I_{exp} over the total current flowing to the cathode I_{tot} in different experimental conditions is plotted. It is shown that at high B_{ext} the whole current is encompassed by the circumference in which the B_ϑ probe lies, therefore confirming that the plasma column extends beyond the corresponding axial position. At low B_{ext} only a fraction of the total plasma current is detected at $z = -109$ mm, with current lines mostly radial linking the cathode to the anode at $z < -109$ mm. Increasing B_{ext} has the effect of axially stretching the current channel, forcing a larger fraction of the current to close at $z > -109$ mm. The lower the B_{ext} value, the lower the ratio I_{exp}/I_{tot}. It is worth noting that the column length shows the same dependence on B_{ext} exhibited by the experimental wavelength in the axial direction, thus allowing to extend to different B_{ext} experimental conditions the validity of the previous assumption of the $n = 1$ mode periodicity. This hypothesis is further confirmed by recent experimental investigations of $m/n = 1/1$ helical instability by means of a fast CCD camera in a similar open system as a coaxial gun device [22]. In this device, where, contrary to the MPD, a direct flux link is always established between cathode and anode, the kink is shown to modify the direction of the current channel from axial to azimuthal, in a paramagnetic process that is demonstrated to amplify the applied B_{ext}.

To explain the generation of magnetic field on the axis, the helical distortion can be approximated as a solenoid of $1/L$ turns per unit length. For the case shown in Fig. 2 the current driven in the solenoid should be 8 kA, which yields a generated B_z of approximately 18 mT, in rather good agreement with the experimental value of 25 mT.

It must be said that the low temperature, high density plasma produced by the HPT, when operating with Argon, has a Lundquist number S between 20 and 400, where $S = \tau_r/\tau_A$, and τ_r and τ_A are the characteristic resistive and alfvénic time scales, of the order of 100 μs and of few μs respectively. Such low values of this key parameter would not allow to apply the ideal MHD theory as has been done before. It is however well known that the range of the applicability of this theory is much larger than what would be theoretically expected [25]. Moreover the results of the experiments at lower density with Helium, characterised by Lundquist number larger than 1000 (usually considered high enough for ideal MHD approximation), have shown that the properties of the plasma fluctuations (frequency and amplitude) do not depend on S, so that non-ideal effects are probably not crucial in determining the plasma dynamics.

The possibility to measure the three components of the magnetic fluctuations in the same position allows to further test the present interpretation of the instability, by investigating the polarisation state of magnetic fluctuations. In a very simple approximation, looking from a fixed z position, the rotating kink can be represented as a straight current structure along the z direction moving on a circular path, at some radial position. The two components of the fluctuating magnetic field laying on the plane of the rotation can thus be evaluated. In Fig. 15 the radial and azimuthal components expected when a current filament carrying 1.5 kA rotates about $r = 37$ mm (upper row) are plotted. This radial position, which is between $r = 41$ mm and

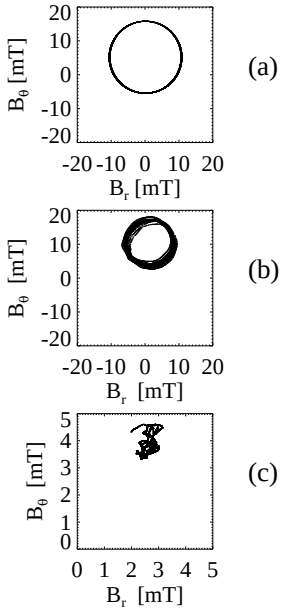

Figure 15. B_r vs B_ϑ) for magnetic probes at $r = 18$ mm: a) theoretical, b) unstable experimental condition with developed kink mode , c) stable condition.

$r = 18$ mm, where the magnetic probes are located, has been chosen because it shows a better agreement with the experimental results. In the same picture the experimental measurements, taken at $r = 18$ mm, for the B_r and B_ϑ are plotted, in two different experimental conditions: with a largely developed $m = 1$ mode (central row), and in a stable case (lower row). In the pictures one component is plotted versus the normal field component (these representations are usually called magnetic hodograms). It is clear that such a simple representation of the rotating kink is in rather good agreement with experimental kink mode results. In particular a regular circular pattern in the (B_r, B_ϑ) plane is displayed by the probes close to the thruster axis, comparable to the 'theoretical' one. When no mode develops very low fluctuations are observed and no regular pattern can be seen.

In a paramagnetic system the q profile is expected to be a decreasing function of the radius and it has already been recollected that the Kruskal-Shafranov criterion [27] prescribes that the q value at the edge of the plasma column must be greater than 1 for the $m/n = 1/1$ stability. This can be written in terms of the parameter $\mu = \mu_0 I/\Psi$, where I is the plasma current and Ψ is the flux of the externally applied axial magnetic field. The stability threshold for the $m/n = 1/1$ mode is thus given by $\mu = 4\pi/L$, and the stability region corresponds to $\mu < 4\pi/L$.

In order to check the applicability of the Kruskal-Shafranov limit to the MPD thruster the μ value for different experimental conditions has been computed, only for $B_{ext} > 0$. In such evaluation Ψ is computed assuming a plasma column radius of 40 mm. The approach for the evaluation of the experimental μ value (μ_{exp}) must be necessarily

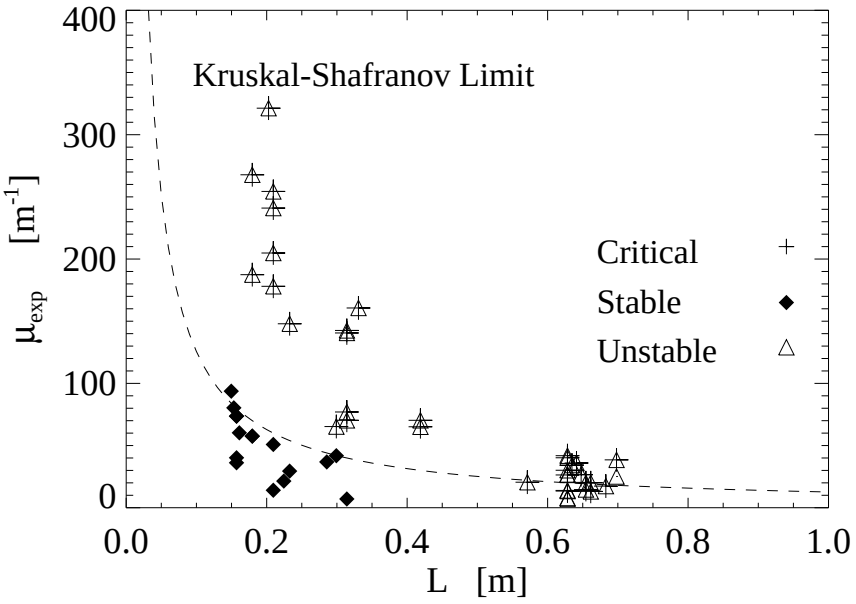

Figure 16. Plot of μ_{exp} as a function of the plasma column length L. Dashed line is the Kruskal-Shafranov limit, which divides stable/unstable regions. Crosses indicate critical regime conditions.

different from the one adopted for the study of the kink instability in the plasma guns for helicity injection, due to the different magnetic topology. In those devices, as already mentioned, a direct linking between the electrodes is established by the magnetic field lines, so that the total plasma current is taken into account in the evaluation of μ. For the case of the HPT, in the formula for μ_{exp} only the experimental current value must be used, as obtained from the B_ϑ measurements.

The μ_{exp} values have been plotted as a function of the plasma column length L, approximated as the experimental λ_z. Stable and unstable cases have been sorted out according to a threshold on the mode energy, namely 10% of the maximum mode energy observed over all the experimental conditions at a given B_{ext} value. The final result is not affected by this choice, due to the fast increase in mode energy observed beyond the stability threshold (see Fig. 12). The result, shown in Fig. 16, shows an excellent agreement with the theoretical Kruskal-Shafranov limit, plotted as a dashed line. In particular, it is interesting to notice that the best agreement is obtained for the shortest estimated column lengths ($L < 0.4$ m). This feature could be related to the strong dependence shown by B_{ext} on the axial position for $z > 0$ (see Fig. 1). At $z > 200$ mm, B_{ext} is mostly radial, so that the description of the thruster plume as a cylindrical plasma column is probably no more valid.

In the same figure the experimental conditions expected to be critical according to the empirical relation (eq. 1) (characterised by the condition $I_{tot} \geq I_{cr}$) are marked with a cross. It is found that critical regimes coincide with cases showing the growth of

the kink mode. Therefore the results confirm that critical regimes are strongly related to the presence of a large MHD kink instability, growing on a $q = 1$ resonant surface in the plasma column [1].

4.2. Kink instability and power losses

It has been shown that the large scale kink modes are probably responsible for the onset of the critical regimes at high current, and therefore they can be considered as the cause of the large wasted energy and reduced thruster efficiency. Figure 17 shows the total energy of the $m = 0, 1$ modes as a function of I_{tot} for the cases with $B_{ext} = 0, 10, 100$ mT. The mode energy is evaluated as

$$E_{tot}(t) = \sum_{m=0,1} [a_m(t)^2] \tag{6}$$

and time averaged over 1 ms during the plateau phase. The corresponding electrical characteristics of the HPT are also plotted [32]. For low B_{ext} values the mode energy is almost zero for $I_{tot} < I_{cr}$ ($\simeq 5.5$ kA) and jumps to high positive values, mainly due to the larger $m = 1$ amplitude, when the current rises beyond the critical value. The agreement between the change of the slope in the ΔV vs I_{tot} curve and the growth of the $m = 1$ mode suggest that this mode is at the origin of the critical regimes, and is responsible for the large power losses and performance deterioration characterising the MPD thrusters at high current regimes.

The analogy with other systems can be extended to understand the power balance issue. In particular, it is known from the experience on RFP [27] and spheromak [33] devices that whenever a kink mode develops a large power is required to sustain the discharge, regenerating the toroidal magnetic flux. RFPs, for example, require an anomalously large loop voltage to drive a given amount of toroidal current. In the past, such voltage anomaly had been interpreted in terms of an enhancement, of unknown origin, of the plasma resistivity. Later it has been shown [27] that the increase in loop voltage is related to the magnetic fluctuations which are responsible for plasma relaxation. These fluctuations are also the main cause of particle and energy radial transport in the plasma core.

The same mechanism, whose physical origin is still object of experimental and theoretical investigation, can be then assumed as responsible for the large power losses and performance deterioration characterising the MPD thrusters operation at high current regimes. In particular, as in other systems, enhanced particle, momentum and energy transport to the walls might be induced by the kink, so that the net axial particles flux, and thus the thrust efficiency, might be reduced.

5. Conclusions

In the present paper an experimental investigation of magnetic, electrostatic and optical fluctuations in the inner part and in the plume of a MPD thruster, both with and without

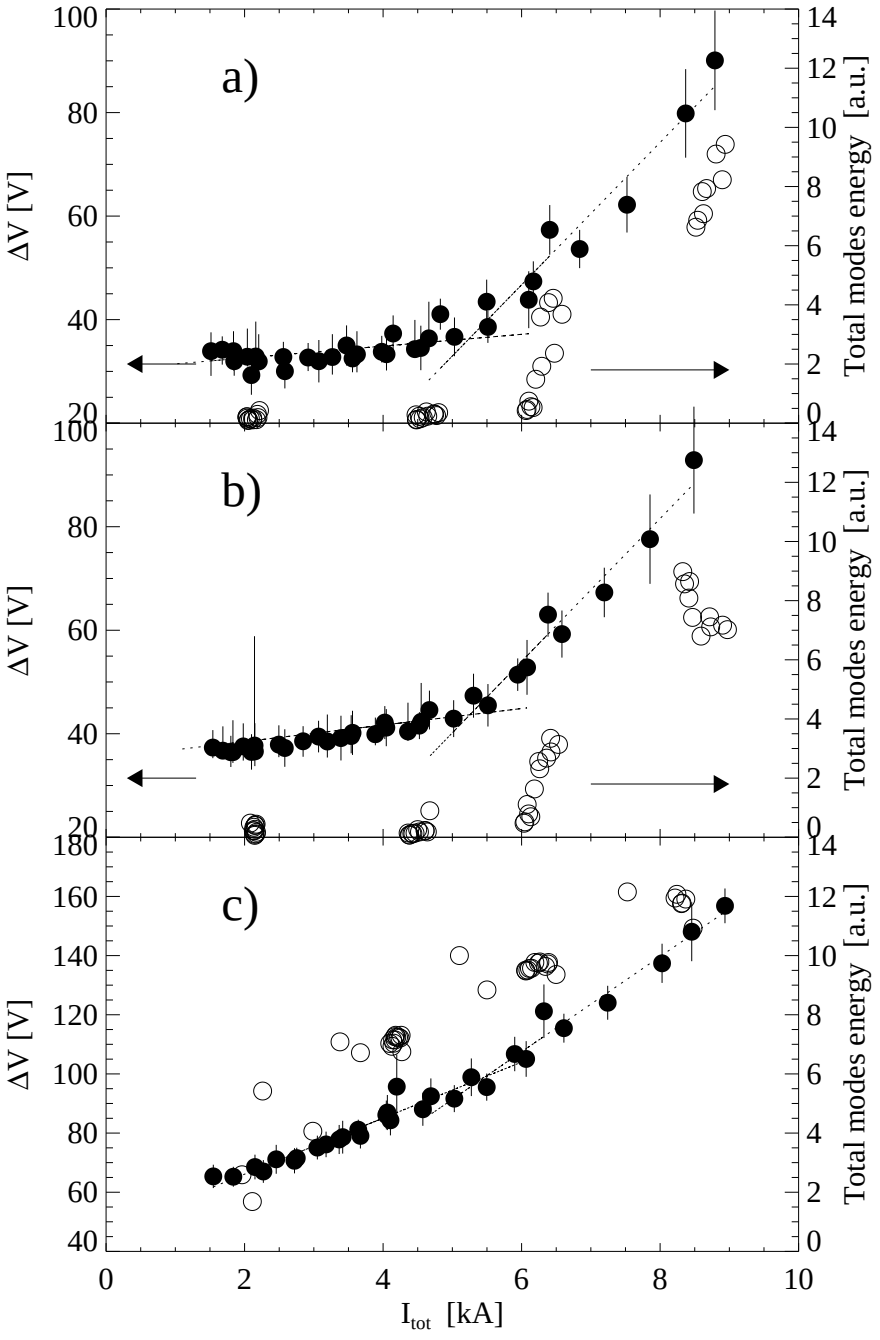

Figure 17. Electrical characteristic (ΔV vs I_{tot}) of the discharge ($\bullet$) and energy of $m = 0, 1$ modes, as a function of the I_{tot}, averaged over time during the plateau phase ($\circ$) for: a) $B_{ext} = 0$, b) $B_{ext} = 10$ mT, c) $B_{ext} = 100$ mT. Dashed lines are linear fittings of critical and non-critical regimes as predicted by eq. 1.

the application of an external axial magnetic field, is described. It has been shown that large scale MHD instabilities develop whenever the current is raised beyond a critical value, which depends on the applied field. The current threshold has been found to coincide with the critical current predicted by a semi-empirical model [5] developed for this kind of thruster.

The instabilities have $m/n = 1/1$ azimuthal and axial periodicity, and are interpreted as helical kink modes. Their growth threshold is in good agreement with the theoretical Kruskal-Shafranov criterion for the instability of the MHD kink mode. Also the presence of a large $m = 0$ mode at some experimental conditions can be described in terms of MHD instability theory (see Ref. [24]). A very simple model proposed for the rotating kink mode is in agreement with the polarisation of the measured magnetic fluctuations. MPDs are shown to exhibit dynamic features similar to those of other systems where a current is driven with a component parallel to an applied magnetic field.

References

[1] M. Zuin *et al.*, Phys. Rev. Lett., **92**, 225003 (2004).

[2] R. G. Jahn, *Physics of Electric Propulsion.* McGraw-Hill Series in Missile and Space Technology, New York: McGraw-Hill Book Company, (1968).

[3] Frisbee, R.H., and Hoffman, N.J., "SP-100 Nuclear Electric Propulsion for Mars Cargo Missions", in 32nd Joint Propulsion Conference, Lake Buena Vista, FL, USA, 1996, AIAA 96-3173.

[4] S. Leifer, "Overview of NASA's advanced propulsion activities", in 34th Joint Propulsion Conference, Cleveland, OH, USA, 1998. AIAA-98-3183.

[5] F. Paganucci *et al.*, Proc. of 27th International Electric Propulsion Conference, Pasadena, CA, 2001 (Electric Rocket Propulsion Society, Fairview Park, OH, USA, 2001) IEPC-01-132.

[6] H. P. Wagner, H. J. Kaeppeler, and M. Auweter-Kurtz, J. Phys. D: Appl. Phys. **31**, 519 (1998).

[7] E. Y. Choueiri, Phys. Plasmas, **6**, 2290 (1999).

[8] D. C. Black, R. M. Mayo, and R. W. Caress, Phys. Plasmas, **4**, 3580 (1997).

[9] R. Hatakeyama, M. Inutake, and T. Akitsu, Phys. Rev. Lett. **47**, 183 (1981).

[10] Y. Amagishi, *et al.*, Journal of the Physical Society of Japan, **71** 2164 (2002).

[11] A. Fruchtman, Phys. Plasmas, **10**, 2100 (2003).

[12] V. B. Tikhonov *et al.*, Proc. of 27th International Electric Propulsion Conference, Pasadena, CA, 2001 (Electric Rocket Propulsion Society, Fairview Park, OH, USA, 2001) IEPC-01-123.

[13] M. Andrenucci *et al.*, Proceedings of 28th International Electric Propulsion Conference, 2003, Toulouse, France, (CNES, Toulouse, 2003) IEPC-03-0301.

[14] M. A. Lieberman and A. J. Lichtenberg, *Principles of Plasma Discharges and Material Processing* (Wiley and Sons, New York, 1994).

[15] P.C. Stangeby, Plasma Physics Series, in: *The Plasma Boundary of Magnetic Fusion Devices* (Institute of Physics, Bristol and Philadelphia, 2000).

[16] G. Serianni *et al.*, 27th International Electric Propulsion Conference, Pasadena, CA, 2001 (Electric Rocket Propulsion Society, Fairview Park, OH, USA, 2001), IEPC-01-135.

[17] C. Hidalgo, Plasma Phys. Control. Fusion **37**, A53-A67 (1995).

[18] R. Cavazzana *et al.*, Rev. Sci. Instrum. **75**, 4152-4154 (2004).

[19] J. S. Bendat, A. G. Piersol, *Random Data, Analysis and Measurements Procedures*, 2^{nd} edition, John Wiley & Sons, New York, 1986

[20] J. M. Beall, Y. C. Kim and E. J.Powers, J. Appl. Phys. **53**, 3933 (1982).

[21] S. J. Levinson, J. M. Beall, E. J. Powers and R. D. Bengston, Nucl. Fusion **24**, 527 (1984).

[22] S. C. Hsu and P. M. Bellan, Phys. Rev. Lett. **90**, 215002 (2003).
[23] M. Nakamura, Y. Uchida, and S. Hirose, New Astron. **6**, 61 (2001).
[24] M. Zuin *et al.*, Phys. Plasmas **11**, 4761 (2004).
[25] J. P. Freidberg, *Ideal Magneto-Hydro-Dynamics*, Plenum Press, New York (1987).
[26] A. J. L. Verhage, A. S. Furzer and D. C. Robinson, Nucl. Fusion **18**, 457 (1978).
[27] S. Ortolani and D. D. Schnack,*Magnetohydrodynamics of plasma relaxation*, (World Scientific, Singapore, 1993).
[28] J. B. Taylor, Rev. Mod. Phys. **58**, 741 (1986).
[29] P. T. Yoon, A. T. Y. Lui and M. I. Sitnov, Phys. Plasmas, **5**, 1526 (2002).
[30] E. G. Harris, Nuovo Cimento bf 23, 115 (1962).
[31] T. J. Gooding, B. R. Hayworth and R. H. Lovberg, AIAA Journal, Vol. 1, No. 6, June 1963, pp. 1289-1292.
[32] M. Zuin *et al.*, 40th AIAA/SME/SAE/ASEE Joint Propulsion Conference and Exhibit, 3473, 11-14 July, Fort Lauderdale, Florida.
[33] P. K. Browning, G. Cunningham, S. J. Gee, K. J. Gibson, A. al-Karkhy, D. A. Kitson, R. Martin and M. G. Rusbridge, Phys. Rev. Lett. **68**, 1718 (1992).